Investigation on the relation between edge radial electric field asymmetries in RFX-mod and density limit

Investigation on the relation between edge radial electric field asymmetries in RFX-mod and density limit

Gianluca Spizzo, Paolo Scarin, Matteo Agostini, Alberto Alfier, Fulvio Auriemma, Daniele Bonfiglio, Susanna Cappello, Alessandro Fassina, Paolo Franz, Lidia Piron, Paolo Piovesan, Maria Ester Puiatti, Marco Valisa and Nicola Vianello

Consorzio RFX, Euratom-ENEA Association, Padova, Italy

E-mail: gianluca.spizzo@igi.cnr.it and paolo.scarin@igi.cnr.it

Abstract

In all major confinement devices (tokamaks, stellarators, spheromaks and reversed-field pinches—RFPs), a density limit has been found. Results summarized in a recent work by Puiatti *et al* (2009 *Nucl. Fusion* **49** 045012) show that in the RFP high density does not cause a disruption, but a sequence of increasingly critical phenomena. First, at intermediate density there is the disappearance of the high-confinement quasisingle helicity/single helical axis regimes. Then, at densities close to the Greenwald limit, toroidally and radially localized density accumulation and radiation condensation are observed, together with a fast resistive decay of the plasma current, which constitutes the real operative limit of the device. In this paper we discuss the effect of the magnetic ripple on test particle motion, showing that the accumulation of electrons in the X-points of the edge $m = 0$ islands is responsible for a modulation of the radial electric field E_r which is at the core of the density limit mechanism. These results can be also relevant for the explanation of X-point multifaceted asymmetric radiation from the edge formation, observed in L-mode density limit discharges of JET.

(Some figures in this article are in colour only in the electronic version)

1. Introduction

The density limit is an operational limit which can be expressed in tokamaks as a function of the Greenwald parameter $n_G = I/\pi a^2$ (n_G in $10^{20}\,\mathrm{m}^{-3}$, I in MA, a in m). Whenever $n > n_G$ disruptive behavior is seen in Tokamaks [1]. Stellarators show a non-disruptive limit which can be well described by the Sudo parameter $n_S = (P \cdot B/a^2 R)^{0.5}$ (n_S in $10^{20}\,\mathrm{m}^{-3}$, P in MW), where P is the power input and B the magnitude of the equilibrium field [2].

In the RFX-mod ($R = 2$ m, $a = 0.459$ m) reversed-field pinch (RFP) [3] we observe a rather complex phenomenology as a function of the density normalized to the Greenwald parameter, n/n_G. First, at $n/n_G \sim 0.35$ the high confinement, good-flux surface quasisingle helicity (QSH) states [4–7] disappear in favor of the low-confinement, multi-helicity (MH) state. Secondly, at densities larger than $\sim 0.35\,n_G$, total radiation and density are increased in the last 10–20 cm of plasma next to the wall [8], in the shape of a toroidally localized, poloidally symmetric ring about $30°$–$90°$ toroidally wide [9, 10]. The radiated power loss plus the increased resistivity due to edge cooling bring about a phenomenology similar to the multifaceted asymmetric radiation from the edge (MARFE) phenomenon in Tokamaks. The MARFE are poloidally localized and toroidally symmetric radiative structures [11] which have been observed in connection with the L-mode density limit, and which can be compared with the RFP radiative rings if one recalls that the parallel direction is poloidal in the edge of the RFP, toroidal in the Tokamak. In contrast to tokamaks, where the latest stage of the MARFE is invariably the destabilization of the $m = 2$, $n = 1$ resistive tearing mode, current quench and disruption [12–14], in RFX-mod the edge cooling and localized radiation does not lead to disruptions, but to the practical impossibility of sustaining the discharge with an ohmic heating limited by the voltsecond stored in the magnetizing circuit [15]. This is the real operative limit of the device, which is reached at $n \sim n_G$.

In this paper we want to explain the edge density accumulation and consequent cooling which is observed at $n/n_G \gtrsim 0.35$ in terms of the magnetic topology near the reversal surface $q = 0$ in the MH state. The discussion of the topological transition between QSH and MH, which happens at $n/n_G \approx 0.35$ and is a precursor of the density limit phenomenology, is still less clear, and is presently under investigation.

The results we will show, together with already published works [9, 10], suggest that transport processes occurring at the edge limit the achievable edge density. For example, in Alcator C-mod it has been shown that the scrape-off layer (SOL) cross-field diffusion plays a critical role [16]. A *critical edge density* has been shown to exist in the Large Helical Device (LHD) [17]. This is in agreement with the fact that density fuelling via pellets and (in the tokamak) strong neutral beam heating lead to peaked density profiles that push the average density beyond the Greenwald limit [18–20]. Studies performed on the TEXTOR limiter tokamak also showed that the edge density is limited due a critical edge density given by the MARFE stability criterion [21, 22]. Being the edge density a critical issue, the wall hydrogen recycling is an important leverage to act on: in the Frascati Tokamak Upgrade (FTU) the Greenwald limit has been overcome by conditioning the wall with lithium, which dramatically reduces recycling and leads to peaked density profiles without the aid of pellets [23, 24]. Similar conclusions on the role of wall recycling over the density limit have been drawn on TEXTOR, where experiments of wall conditioning with boron or silicon and a careful control of plasma equilibrium pushed the density limit up to $n/n_G \simeq 1.7$ [18, 21].

A critical element in our analyses is that edge density accumulation is due to the reversal along $\hat{\phi}$ of the plasma flow toroidal component $v_\phi \sim E_r B_\theta$ averaged in the last 2–3 cm from the wall, when $n/n_G \gtrsim 0.35$ [9]. As soon as v_ϕ changes sign, a strong toroidal particle convection is produced, much larger than perpendicular diffusion in this region. Since the radial electric field close to the wall is thought to be mostly ambipolar, the reversal of the edge flow translates directly in a reversal along $\hat{\phi}$ of the radial electric field. In this paper we will model the E_r reversal along $\hat{\phi}$ by means of the guiding center code ORBIT [25]. We will discuss the radial diffusion of monoenergetic test particles (electrons and ions) subject to the real topology of the magnetic field in the edge of the RFX-mod, and to Coulomb collisions with a background. The result is that we can reproduce an ambipolar electric field that approximates the experimental one, and which is mostly due to a slowing down of electron

radial diffusion near the X-points of $m = 0$ islands [26] resonating at the reversal surface $q = 0$. Electron diffusion is therefore modulated along $\hat{\phi}$. In contrast, ions possess larger drifts and therefore their transport across the X-points is much more uniform along the toroidal angle. In this way, small toroidal differences in the slow motion of electrons in the radial direction (which is the perpendicular direction in the RFP edge) can produce the $\boldsymbol{E}_r$ reversal along $\hat{\phi}$. Collisional effects are comparatively smaller than those due to the magnetic topology at the edge. Besides, we will also shortly comment on the transition in electrostatic transport between a turbulent and collisional regime, which points toward a dominance of collisions at $n/n_G \gtrsim 0.35$.

Our results can be useful also for other magnetic configurations, since the physical mechanism regulating electron perpendicular transport in the RFP edge governs the phenomenological parameter n/n_G, and could in principle constitute a common ground for a unique interpretation of the density limit in tokamak, RFP and stellarator. In particular, we think that our results are relevant for the explanation of the phenomenon of divertor detachment and the X-point MARFE formation, since the reversal of the edge electric field along the perpendicular angular direction is a quite simple explanation for an anomalous density accumulation in the X-point of a divertor-like configuration. In this sense, our suggestion is to look at the poloidal flow v_θ which is the Tokamak analog of the RFP flow v_ϕ that produces the observed density accumulation in RFX-mod.

The paper is organized as follows: in section 2 a review of the known phenomenology of the density limit in the RFX-mod is presented; in section 3 we discuss the results of the simulations of the ambipolar field made with ORBIT. In section 4 the role of turbulence is discussed and finally in section 5 we draw our conclusions.

2. Phenomenology

2.1. Overview of density limit phenomenology

The RFP is a fusion device that exploits a toroidal configuration for plasma confinement with a safety factor profile q monotonically decreasing from the core to the edge, where it changes sign according to the toroidal field reversal which gives the configuration its name (see figure 1). The surface $q(r_{rev}) = 0$ is called *reversal surface* and is characterized by rather peculiar transport properties: it has been shown that, due to the resonance of the $m = 0$ modes, the reversal surface hosts a group of islands with their O and X-points [26] aligned in the toroidal direction at $r \approx r_{rev}$ which reduce ion transport in the RFP edge (a sort of edge 'transport barrier'). In addition to this, the core of the RFP, especially at high current and with the help of the feedback system of active coils [27], shows the development of a helical equilibrium (single helical axis topology, i.e. SHAx regime) which features an internal transport barrier for electrons [4].

The operational space of RFX-mod, density n_e as a function of Greenwald parameter n_G, is shown in figure 2: each data point corresponds to a single discharge, showing that it is difficult to cross the Greenwald limit $n_e = n_G$, and this becomes even more difficult when plasma current is increased. This difficulty in performing high-current, high-density discharges has been interpreted in terms of a fuelling issue [9], but it is also the result of the deliberate operative choice of limiting the ohmic input power. In the previous RFX experiment, density values close to n_G were obtained also at high current ($I_p = 1\,\text{MA}$, which corresponds to $n_G = 1.5 \times 10^{20}\,\text{m}^{-3}$) by ramping the ohmic input power up to 80 MW [28], similar to what is done in tokamaks, where the critical density is pushed up by increasing the input power [18]. In the RFX-mod machine ramping up the input power presently is judged unsafe for the power
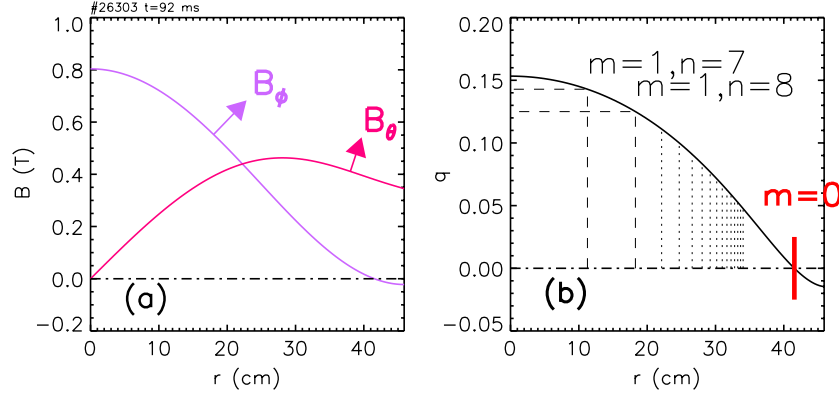
Figure 1. Radial profiles of the equilibrium toroidal B_ϕ and poloidal B_θ component of the magnetic field in a RFP. The reversal parameter of this particular discharge is $F = B_\phi(a)/\langle B_\phi \rangle = -0.1$; (*b*) radial profile of the safety factor profile $q(r)$ calculated in cylindrical approximation. The resonance radii of the $m = 1, n = 7$–8 modes are plotted: the $m = 0$ modes resonate at the reversal radius, $q(r_{\text{rev}}) = 0$.
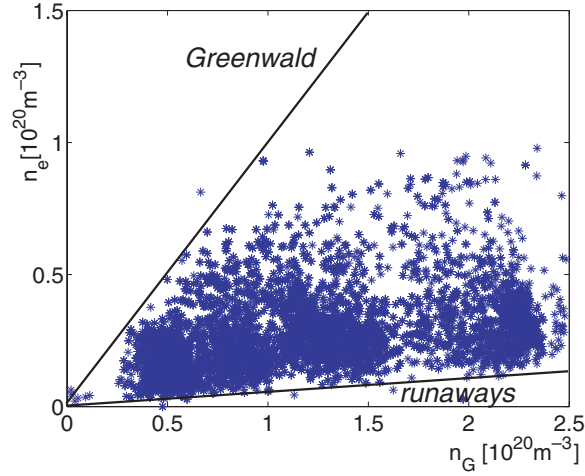

Figure 2. Operational space of RFX-mod expressed in terms of line-integrated density n_e and Greenwald parameter n_G. Discharges remain in the lower portion of the n-n_G plane, and sustaining high-density discharges become more difficult at high currents. As a reference, $n_G = 1.5$ and 2.2 corresponds to 1 MA and 1.5 MA in RFX-mod, respectively.

load on the first wall, and requires the optimization of the plasma current feedback control scheme.

No disruptive behavior is seen in the RFP, in contrast to tokamaks, where the L-mode density limit is often associated with strong MHD activity [1] and the destabilization of the $(m = 2, n = 1)$ mode with consequent disruption [13]. The analogy with the stellarator [2] is more difficult to draw [9], since by re-expressing the Greenwald parameter in terms of the safety factor as $n_G = 5B/\pi Rq$, the stellarator does not follow the Greenwald plot of figure 2. The stellarator shows instead a dependence in terms of heating power, namely the Sudo parameter $n_S = (P \cdot B/a^2 R)^{0.5}$. Nevertheless, we must remark that the heating of the RFP is ohmic, so the plasma current in the RFP has both meanings, average poloidal field $B_{\theta,\text{a}} = \mu_0 I/2\pi a$ and
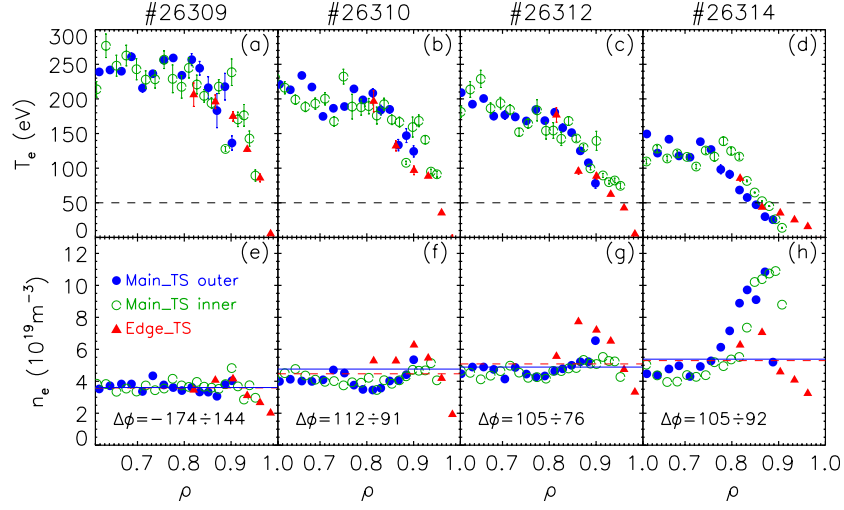
Figure 3. TS profiles of temperature (*a*)–(*d*) and density (*e*)–(*h*) for a series of discharges with increasing n/n_G and keeping constant plasma current $I_p = 800$ kA (left to right, $n/n_G = 0.28$, 0.35, 0.44 and 0.6). Dashed line in (*a*)–(*d*) marks $T_e = 50$ eV; horizontal lines in (*e*)–(*h*) mark the line-averaged density $\langle n \rangle$ measured by the interferometer at the same time. The *x*-axis is the normalized poloidal flux coordinate $\rho = (\psi_p/\psi_{p,w})^{1/2}$; $\Delta\phi = \phi_{TS} - \phi_{lock}$ is the phase relation between the TS toroidal angle and the position of the locked mode (see discussion in section 2.2).

heating power $P = R \cdot I^2$. Thus, it is not possible to ascertain whether we should consider a Greenwald or Sudo scaling.

The reason for the fast plasma current decay has already been shown in a preceding work [10] to be a stronger dissipation due to higher edge resistivity and increased radiated power losses. Results have been summarized in figure 3, where temperature and density profiles, measured by the main [29] and edge [30] Thomson scattering (TS) diagnostics, are plotted as a function of the normalized poloidal flux coordinate $\rho = (\psi_p/\psi_{p,w})^{1/2}$. Panels from left to right in figures 3((*a*)–(*d*) for temperature, (*e*)–(*h*) for density) correspond to four different discharges with increasing density (normalized to the Greenwald density, $n/n_G = 0.28$, 0.35, 0.44 and 0.6) and same plasma current $I_p = 800$ kA. Edge TS density profiles are calibrated absolutely, while those of the main TS are calibrated relative to the corresponding inverted interferometer profiles (for details on the relative calibration of the main TS, see the appendix of [31]).

The inner and outer profiles have been marked by open (○) and full (●) dots, respectively; edge TS data points are shown as full triangles (▲). It is important to underline that we have selected profiles approximately with the same $\Delta\phi = \phi_{TS} - \phi_{lock}$, which is the phase difference between the TS toroidal location and ϕ_{lock}, the toroidal position of the maximum coherent superposition of $m = 1$ MHD modes (often called 'slinky' or 'locked mode' [32]). This choice assures that the profiles correspond to similar magnetic topology, as it will be shown in more detail in section 2.2.

By comparing figures 3(*e*)–(*h*) it is evident that, by increasing core density, the initially flat profile becomes hollow, and finally the edge density exceeds the core value by a factor ∼3. This fact is highlighted by the horizontal lines overplotted on the density profiles in panels (*e*)–(*h*), which indicate the average density $\langle n \rangle$, measured at the same time by the interferometer. This means that the markedly hollow profile is toroidally localized, being not
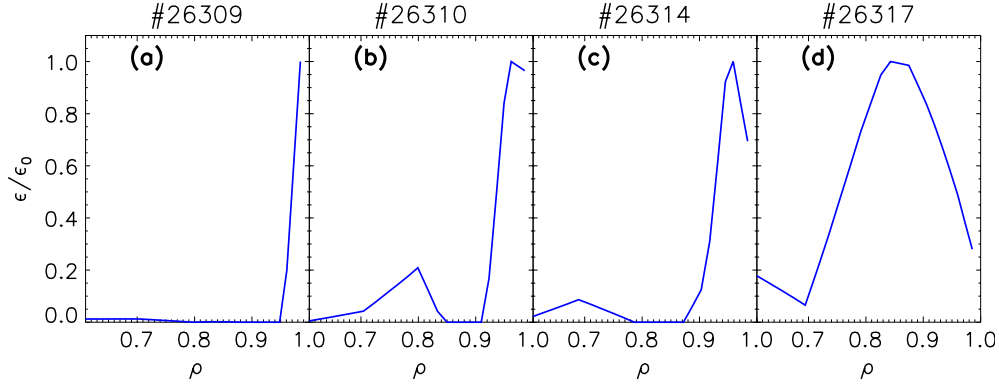
Figure 4. Bolometric emissivity profiles for a series of discharges with increasing n/n_G and keeping constant plasma current $I_p = 800\,\text{kA}$: (*a*) $n/n_G = 0.28$, (*b*) 0.35, (*c*) 0.6 and (*d*) 0.8. Profiles are normalized to their maximum value ϵ_0. The peak shrinks toward the plasma center, similar to the 'radiative contraction' phenomenon seen in L-mode density limit in tokamaks.

detected by the interferometer, toroidally located $60°$ away from the TS. This fact sets also a caveat for the use of the parameter n/n_G: in the case of figure 3(*h*), while $\langle n\rangle/n_G = 0.6$ if one uses the interferometer density, $n_{\text{edge}}^{\text{TS}}/n_G \sim 1.5$ (well above the Greenwald value) if one uses in contrast the toroidally localized edge density measured by the TS. For this reason, in the rest of the paper, n/n_G will be used as a pure phenomenological parameter.

The markedly hollow profile of figure 3(*h*) is poloidally symmetric ($m = 0$, see the good matching between inner and outer main TS profiles) and toroidally localized at $\phi - \phi_{\text{lock}} \sim 100°$. As it is evident by comparing top and bottom rows in figure 3, the density increase is correlated with the widening of the radial region at low temperature ($<50\,\text{eV}$) where low ionization stages of impurities (B, C and O [33]) mainly emit. Consequently, the bolometric emissivity profile shrinks toward the plasma center, as shown in the density scan of figures 4(*a*)–(*d*): this phenomenon resembles the 'radiative contraction' seen in tokamak L-mode density limit [13]. As explained in detail in [9, 10], all these observations are likely explained by a radiative instability which increases resistivity and finally shrinks the current channel: in the classical picture described by Wesson [13, 34], the increase in the density gradient causes an increase in radiated power in the edge layer. Since the radiated power cannot exceed the power input impinging on the edge, the temperature gradient flattens to decrease thermal losses, and the instability grows toward the core. In the Tokamak, this fact leads to a change in the plasma current profile, which destabilizes the $(m, n) = (2, 1)$ resistive tearing mode [14]; in the RFP the plasma current cannot be sustained against resistive diffusion, resulting in a soft-landing of the discharge [10]. In this respect, by exchanging poloidal and toroidal directions, the phenomenon of radiation condensation in RFPs resembles the MARFE in tokamaks [11].

It is worth noting that the phenomenology of the density limit described so far as a function of n/n_G is accompanied by an increase in the $m = 0$ ripple coherence. Define the $m = 0$ phase dispersion parameter [35]

$$\Delta^n = \varphi^{0,n+1} - \varphi^{0,n} - \varphi^{0,1}, \tag{1}$$

where $\varphi^{0,n}$ is the phase of the $m = 0$, n MHD mode. It is straightforward to verify that $\Delta = 0$ corresponds to maximum coherence (constructive interference). In figure 5 we calculate the phase dispersion Δ^n for $n = 1 - 9$ as a function of time during a discharge, and we calculate
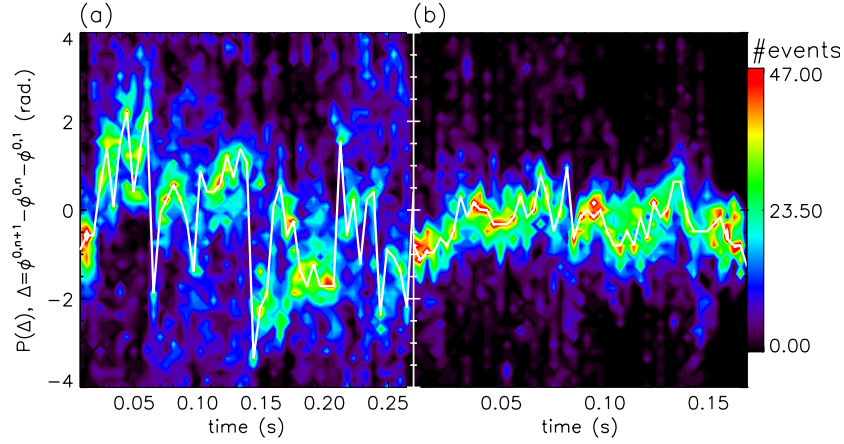
6

Figure 5. Distribution of the $m = 0$ phase dispersion Δ^n, $n = 1 - 9$, as a function of time for two different discharges with (*a*) $n/n_G = 0.17$ and (*b*) 0.52.

the two-dimensional probability of occurrence of a given value of Δ within a 50×50 grid in the time—phase space. While at low density (figure 5(*a*), $n/n_G = 0.17$) the phases are rather dispersed, and only occasionally they are aligned, at high density (figure 5(*b*), $n/n_G = 0.52$) $\Delta^n \approx 0$, $\forall n$ during the whole discharge. At the same time, the $m = 0$, $n = 1–6$ mode amplitude, as a function of n/n_G, increases as well, as shown in figure 6(*a*) for three series of 12 discharges each, performed keeping constant $I = 800$ kA and 1.2 MA, and gradually raising density. In the low-current case ($I = 800$ kA) we also varied slightly the equilibrium, namely the reversal parameter $F = B_\phi(a)/\langle B_\phi \rangle$, maintaining the other parameters fixed: the two equilibria are $F = -0.1$ (solid line) and $F = -0.05$ (dashed–dotted line). The increase in $m = 0$ mode amplitude is mainly due to the first harmonic, $m = 0$, $n = 1$.

We have evaluated the dependence of the $m = 0$ amplitude on equilibrium, namely the reversal parameter, and compared it with the prediction of the nonlinear visco-resistive MHD code SpeCyl [36]. It is observed that the amplitudes in the less reversed case ($F = -0.05$) are systematically lower—more statistics is anyway required to clarify this dependence on equilibrium. Note that, in the high-current case (dashed–dotted and bullets ●) the amplitudes match those of the low-current case with the same equilibrium condition ($F = -0.05$), indicating that equilibrium is more important than current in governing $m = 0$ modes, as predicted in [37].

It is interesting to note that the toroidal displacement $\delta_{m=0}$ due to $m = 0$ modes is simply proportional to the $m = 0$ amplitude through [38]

$$\delta_{m=0}(r, \phi) = -\frac{1}{2\pi r B_\phi} \psi^0(r, \phi), \tag{2}$$

where B_ϕ is the equilibrium toroidal field and ψ^0 is the toroidal flux perturbed by the $m = 0$ modes. It is therefore not surprising that this deformation increases as a function of n/n_G, from ~ 1.5 cm to more than 9 cm. We will see in section 2.3 that the $\delta_{m=0}$ is the convolution of a chain of $m = 0$ islands resonating at the reversal. In this way, the ratio between the maximum $\delta_{m=0}$ and the distance of the reversal from the wall, namely the 'Chirikov wall' parameter $C_w = \delta_{m=0}/(a - r_{rev})$, indicates whether the islands overlap the first wall or not: it will be shown in section 3 that this condition deeply affects the motion of electrons near the wall. The C_w parameter is plotted as a function of n/n_G in figure 6(*b*), and shows that for $n/n_G \gtrsim 0.35$
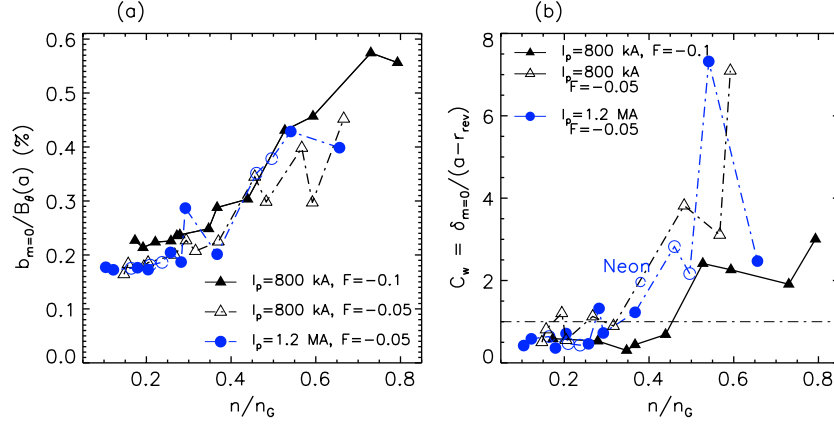
Figure 6. (*a*) Total fluctuation amplitude (toroidal component) of $m = 0$, $n = 1$–6 modes, as a function of n/n_G, for a series of discharges with increasing density, two levels of current ($I_p = 800$ kA and 1.2 MA) and of reversal parameter, $F = -0.05$ and -0.1. The amplitudes have been averaged within the current flat-top phase of the discharge. Solid line (——) corresponds to a series of discharges with reversal parameter $F = -0.1$, dashed–dotted line (— · —) corresponds to another series (same current) with $F = -0.05$. High current discharges have shallow reversal only ($F = -0.05$); (*b*) ratio between the $m = 0$ toroidal displacement $\delta_{m=0}$ and the distance of the reversal from the wall, $C_w = \delta_{m=0}/(a - r_{rev})$, as a function of n/n_G, same dataset as in (*a*). The displacement $\delta_{m=0}$ is calculated with $m = 0$, $n < 24$ modes. In the high-current case, open dots ∘ mark neon-seeded discharges.

the islands overlap the wall. The vicinity of the islands to the wall is therefore a necessary condition for the onset of a radiative instability. This is quite similar to the L-mode density limit behavior in tokamaks [18, 39], where the critical density is determined by the recycling on the wall, and in particular by the size of the gap of the SOL to the inner wall.

In the high-current discharges (bullets and dashed–dotted line), which are usually performed at shallow reversal, the small distance from the wall $a - r_{rev}$ helps in lowering the threshold at $n/n_G \sim 0.25$–0.3, which (partly) explains the observed difficulty in sustaining high-current, high-density discharges in RFX-mod [4]. As a confirmation of this result, a similar analysis performed at lower current ($I_p = 800$ kA) and shallow reversal (triangles and dashed–dotted line) shows a threshold similar to the high-current case.

The increase in the coherence of the $m = 0$ modes as a function of density, and, even more important, the increase in the amplitude of the $(m, n) = (0, 1)$ mode ((0,1) mode in the rest of the paper) is a strong precursor of the density limit phenomenology. As we will show in section 2.3, there is a topological relationship between density accumulation and amplitude of the $(0, 1)$ mode, that is accompanied by the phenomenon of high n islands overlapping the first wall. The sharp increase in $m = 0$ amplitude in a rather narrow density range ($n/n_G \approx 0.4$–0.5) is indicative of a change in regime rather than a continuous scaling, similar to the phase transition between multiple and single-helicity (MH-QSH) states seen in MHD simulations [40]. In this respect, we would underline that, while in figure 6 discharges corresponding to $n/n_G \lesssim 0.35$ show QSH states, all discharges with $n/n_G > 0.35$ are obtained in the MH state. In RFX-mod this threshold is lowered at high current and $F = -0.05$, being in this case $n/n_G \approx 0.25$.

An important experimental test of the importance of the $(0, 1)$ mode will be obtained by carrying out Ultra-low q (Ulq) discharges at high density: preliminary indications (to be confirmed) show that, by removing the reversal surface $q(r_{rev}) = 0$, it is possible to sustain plasma discharges close to (or even to exceed) the Greenwald density [41].

Another important dependence which deserves to be studied in the future is that on the impurity species: neon-seeded discharges apparently show the same phenomenology sketched for hydrogen. In figure 6(*b*) examples with neon seeding at high current are plotted as empty dots (○), indicating that the increase in $m = 0$ modes and island overlapping the wall are only slightly influenced by neon seeding. More analyses are to be performed (especially with helium as a filling gas, which has no chemical reactions with the wall, in contrast to hydrogen); it is worth mentioning that in an old RFP experiment located in Padova, ETA-BETA II ($R = 0.65$ m, $a = 0.125$ m), argon-seeded discharges showed that the high-density limit was shifted to filling densities lower than in pure deuterium [42]. At that time, this phenomenon was interpreted as a balance between ohmic heating and radiation losses.

2.2. Flow reversal in the edge

The radiative instability described in section 2.1 is only the final outcome of a rather complex chain of events eventually producing an accumulation of density, toroidally localized and poloidally symmetric. To study in more detail the phenomenology of this density accumulation, we will consider gas-puff imaging (GPI) [43] and internal system of sensors (ISIS) [44] measurements of toroidal velocity fluctuations v_ϕ, and we will compare them with the total radiated power measured by the bolometric tomography [45]. The propagation of fluctuations in the edge (last $\sim$2–3 cm) of the machine corresponds (within a good approximation) to the $\boldsymbol{E} \times \boldsymbol{B}$ plasma flow itself [46], which is well known to be the only advective term for plasma structures [47]. Since $B_\phi \approx 0$ in the plasma edge, the toroidal velocity is simply proportional to the radial electric field. A limitation of the GPI and the bolometric tomography is that they measure at a fixed toroidal location, ϕ_{diag}: we can anyway obtain a complete toroidal profile (one per discharge) by taking as a reference the (time varying) position of the locked mode, ϕ_{lock}, and transforming time into toroidal angles through $\phi = \phi_{\text{diag}} - \phi_{\text{lock}}(t)$ (for details, see [10]). It has been already shown in the past that the plasma flow displays regular patterns as a function of the locking angle [48, 49].

The toroidal profile of plasma flow is given in figure 7(*a*) for a high-density discharge ($n/n_{\text{G}} = 0.8$), and shows the presence of two null points: a source at $\phi = \phi_{\text{lock}}$ and a sink (stagnation point) at $\phi - \phi_{\text{lock}} \sim 100°$. We observe that the reversal of v_ϕ along the toroidal direction $\hat{\phi}$ conveys the edge robust toroidal flux ($\approx 10^{23}$ m^{-2} s^{-1}, much larger than the radial diffusive flux, $\approx 10^{22}$ m^{-2} s^{-1}) to the stagnation point, where density accumulates, temperature decreases, resistivity increases and plasma emits radiation. In fact, in figure 7(*b*) we see that most radiation is localized toroidally at the stagnation point, and is poloidally symmetric ($m = 0$). A fainter toroidal peak is present at $\phi = \phi_{\text{lock}}$: in fact, it is a well-known result in the RFP that the locking angle of $m = 1$ modes is a preferential source of particles and localized plasma–wall interaction [50], as confirmed by H_α measurements in discharges similar to that shown in figure 7 (see, e.g., figure 4(*e*) in [9]). In this way, the natural phase relation between $m = 0$ and $m = 1$ modes causes the source of particles to coincide with the null point of v_ϕ at $\phi = \phi_{\text{lock}}$.

As a comparison, figures 7(*c*) and (*d*) show the plasma flow v_ϕ and total radiation, respectively, for a low-density discharge ($n/n_{\text{G}} = 0.1$): no signature of flow inversion is visible, v_ϕ is always negative. This corresponds to a negative radial electric field averaged in the last 2–3 cm next to the wall, $\langle E_r(r, \phi) \rangle_r = v_\phi \cdot B_\theta$. Correspondingly, total radiation is rather uniform along $\hat{\phi}$, and is concentrated in a $\sim$3 cm wide layer close to the wall. The comparison between panels (*b*) and (*d*) in figure 7 clarifies the mechanism of the radiative instability: by increasing density, radiation condensates toroidally at $\phi - \phi_{\text{lock}} \sim 100°$, and radially forms a
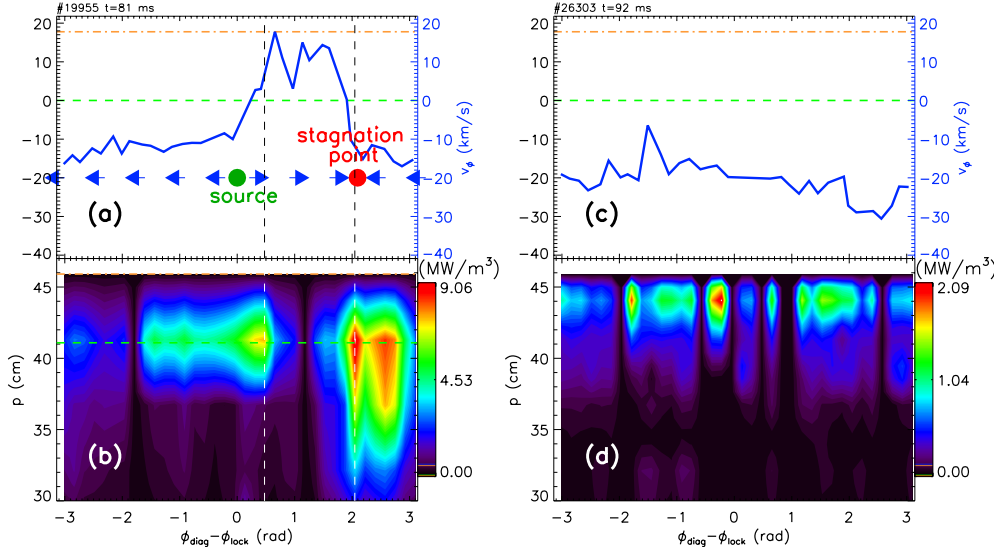
Figure 7. Toroidal patterns of total radiation and plasma flow: (*a*) plasma flow as a function of the toroidal angle, $\phi - \phi_{lock}$, for a discharge with $n/n_G = 0.8$; (*b*) for the same discharge, map of total radiation (minor radius as *y*-axis); (*c*) plasma flow and (*d*) total radiation in a discharge with $n/n_G = 0.1$. Plasma flow has been measured by the GPI diagnostic.

ring that widens and shrinks towards the core, following the temperature contraction shown in figures 3(*a*)–(*d*) and figure 4.

To confirm the flow reversal at high density we considered the measurement of floating potential coming from the toroidally distributed probe system of ISIS [44]. The velocity at different toroidal positions is computed using the cross-correlation technique [51, 52] applied on different groups of five electrostatic pins each pertaining to ISIS. Indeed, the cross-correlation between the pins, calculated every 1.5 ms, exhibits a maximum which presents an almost linear dependence of the time delay on the probe position: this is a signature of toroidal propagation. The five pins cover an angle of approximately 20° toroidally, corresponding to approximately 80 cm and the obtained velocity is assumed to represent the velocity at the center of this region. We repeated this analysis at three toroidal locations: the location closest to the bolometers ($\phi = 213.9°$, squares ■), a location 110° forward ($\phi = 323.9°$, stars ⋆) and one 70° backward ($\phi = 143.9°$, full dots ●). This allows to follow a rough, 3-point toroidal profile of edge flow $v_\phi(\phi_i, t)$, $i = 1$–3, but with the space–time evolution that is lacking in the analysis of the GPI. The results are shown in figure 8(*b*), for a discharge with $n/n_G = 0.8$: the velocity at $\Delta\phi = \phi_i - \phi_{bolo} = 110°$ forward (stars ⋆) is negative at all times. In contrast, the velocity at the bolometer (squares ■) is positive just before the radiation peak (figure 8(*a*)), the latter occurring when the flow changes sign (stagnation point). The flow at $\Delta\phi = -70°$ also shows a positive bulge that anticipates that measured at the bolometer. This confirms that the radiation condensation is correlated with the phenomenon of the stagnation point, as inferred previously from GPI measurements, the absolute values of v_ϕ measured by ISIS and GPI being well compatible.

2.3. Flow reversal and magnetic topology

The phenomenology of the flow reversal can be linked to the magnetic topology in the edge of the RFP, even if this dependence is not peculiar of this magnetic configuration only: recently,
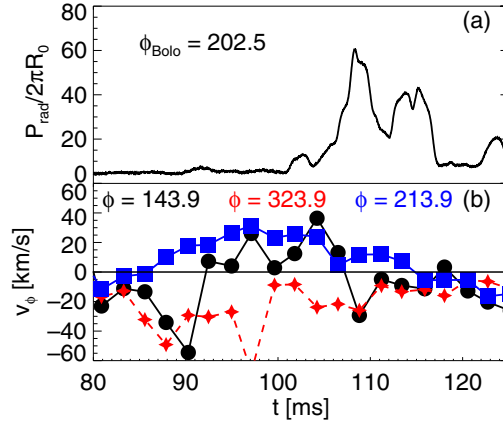
Figure 8. (*a*) Time evolution of total radiation P_{rad}; (*b*) toroidal flow velocity measured by the ISIS sensor system at three toroidal locations, $\phi = 213.9°$ (full squares ■), $\phi = 323.9°$ (stars ★) and $\phi = 143.9°$ (bullets ●). Discharge # 26317, $n/n_G = 0.8$.

cases of E_r reversal have been connected to the operation of the resonant magnetic perturbation (RMP) in the Mega-Ampère Spherical Tokamak (MAST) [53]. A positive electric field $E_r > 0$ was observed also in the perturbed edge of Tore Supra with the use of the ergodic divertor [54], and more recently in TEXTOR with the dynamic ergodic divertor (DED) [55, 56]. In the edge of the RFP the presence of the reversal surface, $q(r_{rev}) = 0$, causes the reconnection of the $m = 0$, $n \geqslant 1$ tearing modes. These modes produce a chain of islands that act as a barrier for electron and ion transport [26]. Therefore, a dependence of the edge toroidal flow on the $m = 0$ modes can be *a priori* expected. Moreover, observations of a dependence of flow/radial electric field on the $m = 0$, $n = 1$ mode have been already reported in the past on RFX [48, 49, 57].

Let us consider the same discharge of figures 7(*a*) and (*b*), and over-plot on panel (*a*) the Poincaré map of the magnetic field (equilibrium plus $m = 0$ islands). Let us start with the first harmonic only, the $m = 0$, $n = 1$ mode: figure 9(*a*) shows that the stagnation point corresponds to the X-point of the (0,1) island. A known result of classical mechanics is that orbits (=magnetic field lines) take infinite 'time' (i.e. infinite length along the field) to perform a complete excursion around the X-point in the vicinity of the separatrix ('homoclinic tangle'). This can be seen by evaluating the period of the orbit near the separatrix in the integrable Hamiltonian which is obtained in a RFP magnetic equilibrium perturbed by a *single* $m = 0$, $n = 1$ mode, namely [58]

$$t = \frac{1}{\sqrt{A}} \log\left[\tan\left(\frac{\pi}{4} + \frac{\zeta}{4} \right) \right]. \tag{3}$$

Here A is a mode 'amplitude' (proportional to the normalized radial fluctuation amplitude $\tilde{b}_r/B_\theta(a)$) and ζ is the (toroidal) angle between the O- and X-points of the island. It is evident that, for half a period of oscillation, $\lim_{\zeta \to \pi} t = +\infty$, namely field lines take an infinite length to fluctuate in the vicinity of the X-point. This behavior affects principally electrons, that at the first order follow field lines, and therefore spend more time in the vicinity of the X-point than elsewhere. In this way, the X-point itself becomes a cause of unbalance in the motion of electrons and ions, so it must have a role in determining the ambipolar field in the edge.

Now add all the $m = 0, 1$ and $|n| = 1$–23 modes in the MHD spectrum, as shown in figure 10(*a*): the X-point of the (0,1) island is no more visible in the Poincaré map. In its place, a chain of $m = 0$ islands is evident, with their O-points aligned in the vicinity of the
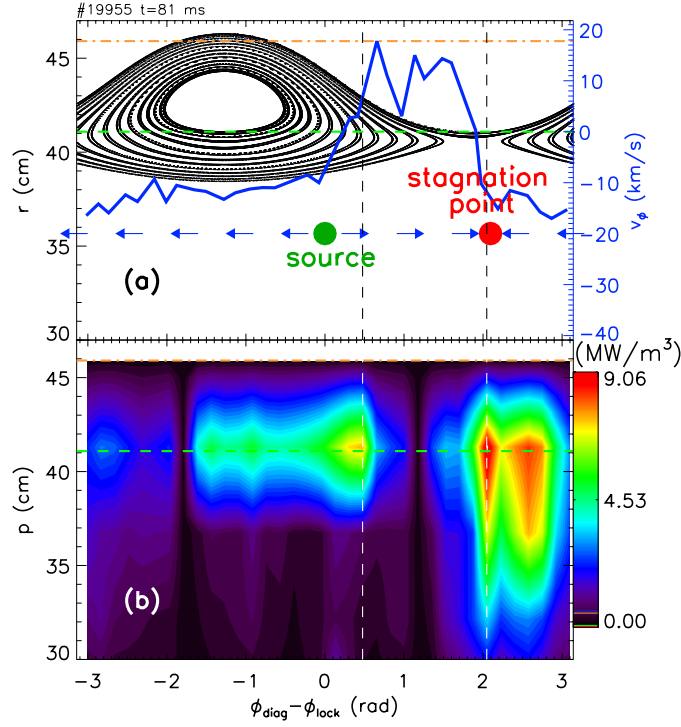
Figure 9. Toroidal patterns of total radiation and plasma flow: (*a*) plasma flow as a function of the toroidal angle, $\phi - \phi_{\text{lock}}$, for the same discharge as in figures 7(*a*) and (*b*). In panel (*a*) the Poincaré plot of the island associated with the $m = 0$, $n = 1$ mode is also shown. The stagnation point for the plasma flow corresponds to the X-point of the island. As a reference, the reversal is plotted as a horizontal, dashed line.

unperturbed reversal (horizontal, dashed line), and shifted outward or inward according to the toroidal modulation of ψ_{p} (which is proportional to the modulation $\delta_{m=0}(\phi)$, shown in figure 6). At $\phi < \phi_{\text{lock}}$ the islands are pushed toward the wall (dashed–dotted line), while at $\phi > \phi_{\text{lock}}$ they are shifted toward the axis. Even if the X-point of the (0,1) mode is no more visible, X-points (in contrast to O-points) possess *structural stability* [59], i.e. a perturbed X-point remains an X-point. In this way, the ability of the X-point to accumulate electrons should remain unchanged. This point is a subject of future work, for example, by calculating the Poincaré recurrence time T_{p} of orbits near the X-point. While this is a simple task in an integrable Hamiltonian with $m = 0$ modes only, equation (3), it becomes rather difficult when we simulate the full MHD spectrum, comprising also $m = 1$ modes, which cause stochastization of the region around the X-points of the (previously) conserved $m = 0$ islands (for details on the Hamiltonian of the $m = 0$ island chain, see [26]).

3. Test particle simulations

The problem of the determination of the ambipolar electric field at the edge of a fusion plasma is a classical one. Simplified analytical calculations, such as those contained in [60], already show the complexity of the topic: different electron and ion perpendicular diffusion in a sheath next to the wall gives rise to an ambipolar field which tends to balance the fluxes. The ambipolar
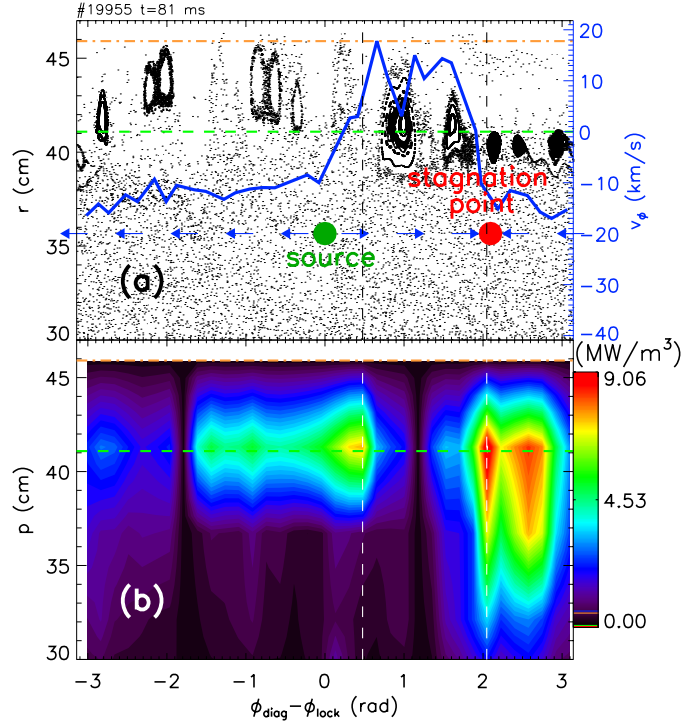
Figure 10. Toroidal patterns of total radiation and plasma flow: (*a*) plasma flow as a function of the toroidal angle, $\phi - \phi_{\text{lock}}$, for the same discharge as in figure 7. In panel (*a*) the Poincaré plot of the islands corresponding to the full $m = 0$ spectrum is shown.

ion flux in the sheath can be written as [60]

$$\Gamma_i^{(a)} = -D_i \nabla n + n\mu_i E_a \simeq n\mu_i E_a \simeq -\frac{T_e}{m_i \nu_{i,b}} \nabla n, \tag{4}$$

with $Z = 1$, m_i the ion mass and $\nu_{i,b}$ the collision frequency of ions with the background. The ion flux to the wall can be written as

$$\Gamma_i^{(w)} = (1 - R_i)n_w \nu_i = (1 - R_i)n_w \sqrt{\frac{T_e}{m_i}}, \tag{5}$$

where it is assumed $T_i = T_e$, n_w is the density at the wall and R_i is the hydrogen recycling coefficient with the wall. Since by definition it must be $\Gamma_i^{(a)} = \Gamma_i^{(w)}$ it is clear that the recycling R_i couples the value of density and temperature in the sheath, n_w and T_e, with the ambipolar field E_a, which in turn is linked to the density gradient and ion collisions. Recycling, edge density and temperature, and ambipolar field should then be calculated in a self-consistent way. The addition of a complex magnetic topology, such as that of the RFP edge, makes the self-consistent analytical calculation of the ambipolar electric field practically impossible, so that we will make a numerical estimate in a simplified condition. From the point of view of experiments, changing the recycling is an important leverage to change the edge density gradient and electron temperature, e.g. with lithium wall conditioning [23, 24].

In our numerical approach we freeze down the kinetic part of the problem, namely the density profile and the recycling are given, and we study the radial motion of test particles (electrons and hydrogen ions H$^+$) embedded in a fixed magnetic topology and subject to
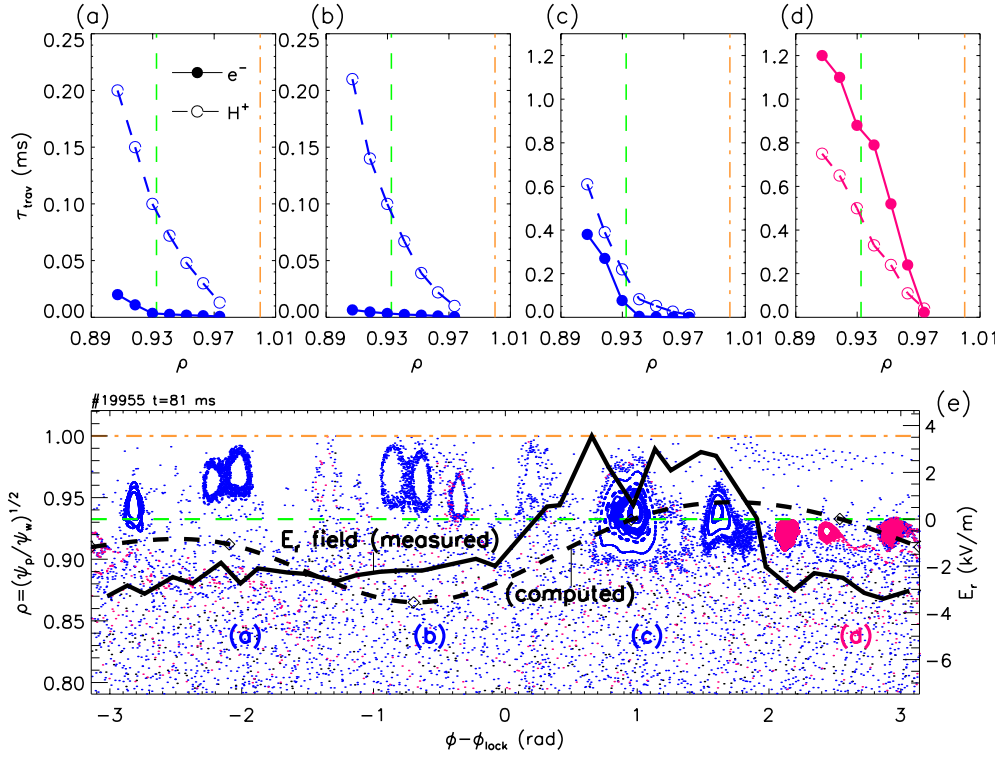
Figure 11. (*a*)–(*d*) Travel times as a function of ρ for particles deposited at $\rho = 0.98$ and at toroidal angles corresponding to the labels (a)–(d) in frame (*e*); (*e*) Toroidal Poincaré plot with measured (solid) and computed (dashed) electric field.

collisions with the background, by making use of the Hamiltonian guiding center code ORBIT [58]. For the magnetic field we use as input the eigenfunctions calculated from the Newcomb's equations in toroidal geometry [61]. Collisions are calculated taking into account C^{4+} and O^{6+} impurities, which are important especially for ion collisions: the background temperature corresponds to a discharge with $n/n_G = 0.8$. Test particles are monoenergetic and are supposed to come from the core, and therefore have been given energy $E = 260$ eV, consistently with the profile shown in figure 3(*a*).

Figure 11(*e*) shows the Poincaré plot (toroidal angle ϕ as x-axis, ρ as y-axis) for the discharge #19955 ($n/n_G = 0.8$), at the time of the density peak (the same as in figure 10(*a*)). Letter (*d*) in figure 11(*e*) corresponds to the X-point of the (0,1) island of figure 9(*a*); we have also overplotted as a solid line the radial electric field $E_r = v_\phi \cdot B_\theta$ corresponding to the flow of edge fluctuations measured by the GPI. The magnitude of the electric field, -2–4 kV m^{-1} in the non-reversed region, is consistent with probe measurements in the old RFX machine [62].

The technique used to diagnose the radial motion of electrons and ions has been already used in RFX [63], and consists in depositing particles in the edge and at different toroidal locations, marked by the letters (*a*)–(*d*) in the Poincaré plot. We remind the reader that in the RFP edge the parallel direction is poloidal, $\hat{\theta}$, the perpendicular directions are radial and toroidal ($\hat{r}, \hat{\phi}$). Moreover, we expect that perpendicular diffusion is mainly radial, toroidal diffusion is quite small since $B_\phi \simeq 0$. The ORBIT code has been upgraded in order to take into account a recycling wall (in its standard configuration ORBIT has a perfectly absorbing

Table 1. Typical values of electron and ion travel times (ms) in X- and O-points, in MH and QSH states.

Run	$\tau_{\text{trav,e}}$ (ms)		$\tau_{\text{trav,i}}$ (ms)	
	O-point	X-point	O-point	X-point
QSH	0.01	0.12	0.18	0.40
MH	0.013	1.20	0.20	0.75

wall, suitable for studies of fast particle and beam losses [25]). Particles are deposited at $\rho = 0.98$ and allowed to diffuse radially, under the action of magnetic field and collisions with the bulk ions/electrons. If a particle (electron or ion) hits the wall, it is lost and replaced by a new particle, at a distance of one gyroradius from the wall and with a new random pitch (normalized parallel velocity $\lambda = v_\parallel / v$). This choice is a schematic modeling of the sputtering processes at the first wall, which include a charge-exchange and subsequent ionization process of a neutral atom [22], in the framework of a single-particle code, which requires particle and energy conservation. The scheme we have devised is more realistic than simply assuming that the wall reflects particles with an elastic collision, like a billiard. This latter case can be reproduced by changing pitch sign when the particle hits the wall. Although this scheme works reasonably well for ions, electrons are reflected back more or less on the same field line (due to their small gyroradius), and end up bouncing to-and-fro in the vicinity of the wall.

As an observable of the radial transport we consider the 'travel time' τ_{trav}, i.e. the time spent by 50% + 1 particles to travel a prescribed radial distance from the initial deposition point.

The travel times for electrons and ions are shown in figures 11(*a*)–(*d*). Electron radial losses are much larger than ions in (*a*) and (*b*), since the corresponding islands in the Poincaré plot in figure 11(*e*) act as a short-circuit for their trajectories; ions are comparatively less mobile and reflect less the magnetic topology due to their larger drifts. The fact that islands close to the wall act as short-circuit for electron transport is consistent with the local flattening of the radial electron temperature profile measured across the islands (see figure 5 in [64]) and reflects the behavior of the toroidal displacement $\delta_{m=0}$, shown in figure 6(*b*). As a consequence, a cloud of positive charges forms next to the wall, and as a result the ambipolar field would be directed inward, which is the usual condition on the RFP [62].

This picture is anyway drastically changed in the vicinity of the small islands in (d), which mark the former X-point of the $m = 0, n = 1$ island of figure 9(*a*): here $\tau_{\text{trav,e}} > \tau_{\text{trav,i}}$ since electrons follow at the first order the field lines and, according to equation (3), spend a lot of time in the vicinity of the X-point, while ions have much larger drifts and their motion is almost unaffected with respect to the O-point of the (0,1) mode. As a reference value, the difference in electron travel time between the X- and O-points is about two orders of magnitude (0.01 and 1.2 ms), whereas in the ion case is only a factor $\sim$3 (0.2 and 0.75 ms), as shown in table 1. If we make a rough estimate of the radial electric field required to balance the fluxes

$$E_a = \frac{1}{n} \frac{\Gamma_e - \Gamma_i}{\mu_i - \mu_e} \propto \frac{1}{\tau_{\text{trav,i}}} - \frac{1}{\tau_{\text{trav,e}}}, \tag{6}$$

provided $\mu_e \gg \mu_i$, we obtain the dashed curve in figure 11(*e*). This ambipolar, radial electric field is negative almost everywhere, except for a region at $\phi > \phi_{\text{lock}}$ where it is positive, and approaches the measured E_r. It is worth underlining that the ambipolar ion flux in the sheath Γ_i is radial, and therefore perpendicular to the magnetic field.

On the basis of these results we may conclude that the ambipolar field given by classical arguments of single-particle motion can account for the electric field required for the edge

flow reversal: this fact suggests that, at the same time, turbulent transport is weakened, as it will be proposed in section 4. Here we want to underline some important aspects of our simulations. First, the wall recycling is important in determining the correct sign of E_r: with a perfectly absorbing wall, the sign of E_r is reversed. This means that neutrals are released more or less in the same toroidal location where the ions are preferably lost from the plasma, in such a way that the recycling pattern reproduces the magnetic pattern of O- and X-points. It is worth mentioning that in TEXTOR the MARFE disappeared by applying a 1 kHz ac magnetic perturbation with the DED, while it appeared again in the case of fixed X-points (dc operation): this fact was explained in terms of rotation frequency of the DED X-points, which in the ac case was larger than the neutral desorption rate from the wall, allowing for smoothing the recycling pattern at the wall [65]. Secondly, our simulations add a new aspect to the MARFE theory. In tokamaks the MARFE is unstable when the edge density exceeds a critical edge value $n_a^{(cr)} \sim \sqrt{\kappa_\parallel/D_\perp}$, proportional to the ratio between the parallel heat transport coefficient and perpendicular diffusivity [22]. Whenever the heat transport from the core is not able to balance thermal losses due to charge exchange/ionization, a MARFE occurs. In the RFP, we have shown that a new, critical element is the ratio between the two perpendicular transport terms, radial diffusion and toroidal convection, $D_r/v_\phi L_n$ (with L_n the density gradient characteristic length). While $m = 0$ islands naturally provide a small D_r term (ORBIT gives an ambipolar $D_{r,a} = 2–4 \, \mathrm{m^2\,s^{-1}}$ in the cases (*c*) and (*d*) of figure 12), toroidal convection (if present) is always very large: with $v_\phi = 10 \, \mathrm{km\,s^{-1}}$ and $L_n \sim 2 \, \mathrm{cm}$ [66], $v_\phi L_n \sim 100 \, \mathrm{m^2\,s^{-1}}$. This can be a caveat for the tokamak, where similar values of $v_\theta L_n$ can easily exceed radial diffusion.

To test the consistency of this interpretation, we consider the reference case, a QSH discharge with $I_p = 800 \, \mathrm{kA}$, $F = -0.1$, $n/n_G = 0.17$, where we know that the radial electric field is constant and negative along the toroidal angle, as shown in figures 7(*c*) and (*d*). The toroidal Poincaré plot is shown in figure 12(*b*). It is noteworthy that a chain of $m = 0$, $n = 7$ islands is still visible in the edge, as found in [67]. In fact, the (0,7) mode arises as a coupling of the single $m = 1$, $n = 7$ mode that dominates the spectrum and toroidicity. The radial width of the islands, 5–7 cm, is comparable to the MH case. In fact, even if the overall $m = 0$ amplitude is substantially lower in QSH by definition [40], the amplitude of the 'secondary' modes with $m = 1$, $|n| > 7$ is also lower, the latter contributing for the reduction in the island size by nonlinear coupling in the Hamiltonian equations of the field line evolution [26]. The main difference between QSH and MH regarding edge topology is the absence in QSH of the $m = 0$, $n = 1$ mode, which introduces the strong toroidal asymmetry visible in figure 11(*e*): in QSH the chain of islands is uniform, with the X- and O-points aligned along the reversal.

Now perform the same exercise as in MH: deposit ions and electrons at $\rho = 0.98$, and different toroidal angles, namely the positions of the X and O-points of the (0,7) islands, and record the transit time τ_{trav}. The travel times for electrons and ions are shown in figure 12 (top row) for two couples of X and O-points, marked in panel (*b*) on the Poincaré plot. It is interesting to note that the mechanism of the X-points acts in a similar way for (0,7) islands in QSH and the (0,1) island in MH: while ion travel time is similar in the O- and X-points (a factor 2 difference, between 0.18 and 0.4 ms), electron travel time is larger in the X-point by one order of magnitude ($\sim$0.12 ms compared with $\sim$0.01 ms, see also table 1). The 'X-point' effect in QSH is anyway milder than in MH, and the resulting E_r field calculated according to equation (6) is *negative everywhere* (electron transit time is always smaller than ion's, see solid line in figure 12(*b*)). The sign of E_r fits nicely experimental results [62, 68], giving at the same time a picture more complex than the finite Larmor radius (FLR) effect, which has been a paradigm for explaining the negative edge electric field for some years [69]: in our case, the charge imbalance is strongly determined by the complex magnetic edge topology.
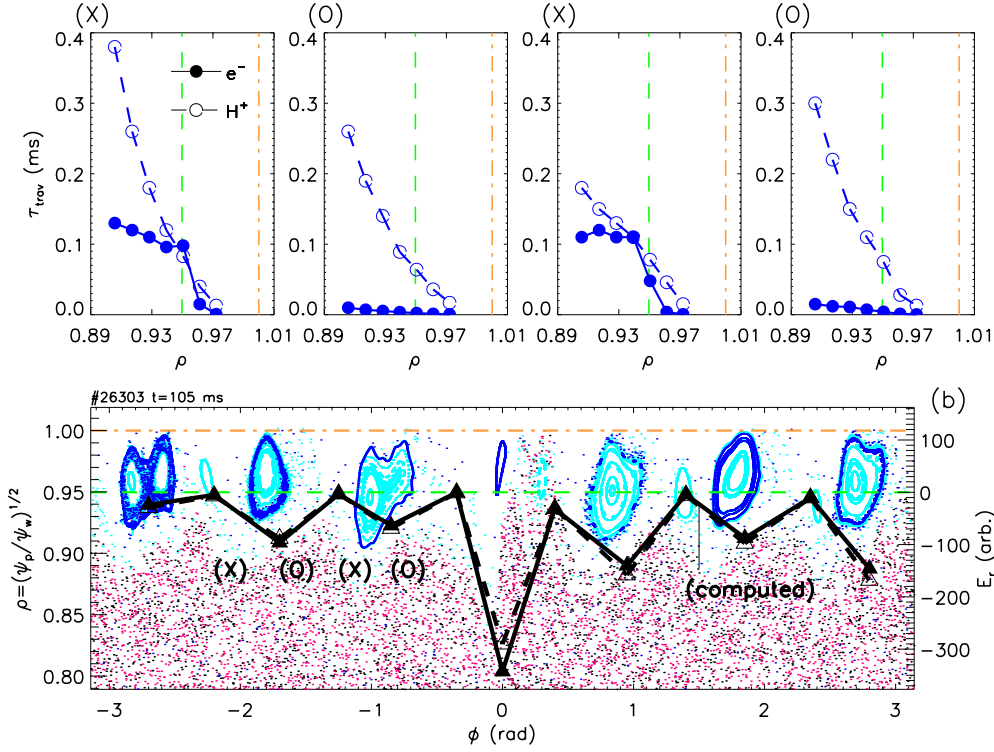
16

Figure 12. (Top) travel times as a function of ρ for particles deposited at $\rho = 0.98$ and at toroidal angles corresponding to two couples of X- and O-points of the $m = 0$, $n = 7$ islands, marked with the same symbol in panel (*b*); (bottom, (*b*)) Toroidal Poincaré plot with computed electric field. The solid line is the case with collisions pertaining to the QSH shot shown in the Poincaré, the dashed line with QSH topology and MH collisions.

The different behavior of electrons in the X-points anyway brings about a modulation of the negative E_r field with the same periodicity of the $n = 7$ dominant mode. This modulation predicted by ORBIT simulations has two experimental counterparts. The thermal helium beam measures a variation of electron pressure modulated seven times along the toroidal angle [70], while ISIS shows the same modulation of the floating potential as a function of time and toroidal angle. The role of the X-points in QSH is matter of future studies, but is likely to be closely related to the QSH–MH back transition that is associated with the observed reversal of E_r.

A final remark is about the role of collisions: since the back transition QSH–MH happens together with a change of collisionality, it is worth testing whether the E_r reversal is dominated by the change in edge topology or collision frequency. We repeated the QSH scan, but using the collision frequency typical of a MH state (see table 2 for the values used in the simulations). The resulting edge electric field is plotted as a dashed line in figure 12(*b*), showing that collisional effects are weaker than MHD-induced topological effects.

4. Role of turbulence

In section 3 an explanation of E_r has been provided in terms of the ambipolar field required by the topological change associated with the QSH–MH transition. The results we presented

Table 2. Collisions (electrons and ions) used in the QSH and MH runs. Collision frequency is normalized to the transit time, $\tau_{tor} = 2\pi R_0/v_{th}$. Collision frequencies are summed up on electron, ion and impurity encounters.

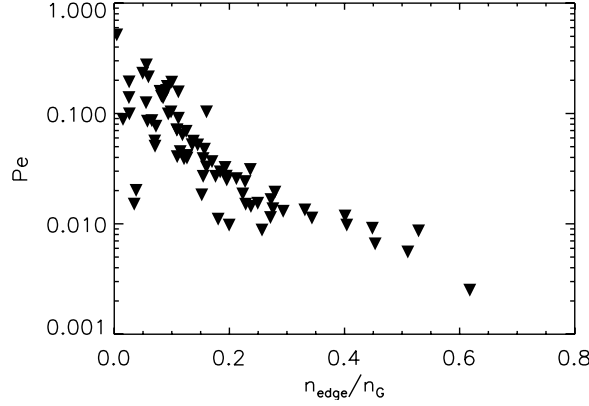| Run	$\nu_e \tau_{tor}$	$\nu_i \tau_{tor}$
QSH (#26303)	1.56	0.97
MH (#19955)	1.42	2.27

Figure 13. Parameter $Pe = \tau_{e,i}/\tau_{tr}$ as a function of density divided by Greenwald density.

have been obtained in the framework of single-particle motion, so we can expect that at high density the role of single-particle motion remains essential.

In fact, an important experimental result is the dependence on collisionality of the particle trapping process by blobs . We define as an indicator the ratio $Pe = \tau_{e,i}/\tau_{tr}$ [71] between electron–ion collision time and transit time $\tau_{tr} = L_\phi/\tilde{V}$ during which a particle with velocity $\tilde{V}$ goes through a blob correlation length L_ϕ. This velocity $\tilde{V}$ is the relative velocity of space-structured blobs embedded in a stochastic background, as measured by the GPI diagnostic [46]. In figure 13 we show Pe as a function of n_{edge}/n_G: this parameter falls off from 0.5 to 0.01 when $n_{edge}/n_G \gtrsim 0.35$, corresponding to a change from 2 to 100 electron–ion encounters per transit time. Numerical predictions of turbulent transport as a function of collisionality [71], showing that at high density, collisions scattering particle trajectories are dominant in comparison with particle trapping within blobs, which in contrast is dominant at low density. At the same time, the global effective diffusion (collisional + turbulent) increases with density.

5. Summary and conclusions

The density limit in the REP is similar to the MARFE phenomenon in tokamaks, being at the same time non-disruptive like in stellarators, and can be parametrized in terms of the Greenwald density $n_G = I/\pi a^2$. The reversal of the toroidal plasma flow along the toroidal angle in the last 2–3 cm of plasma next to the wall has a key role in the density limit phenomenon, because it conveys a robust toroidal flux to a stagnation point. The reversal of the plasma flow is in turn linked to the reversal of the radial electric field next to the wall, which can be well described by the ambipolar constraint. In this respect, the origin of the whole chain of events leading to the density limit is the accumulation of electrons in the vicinity of the X-point of the $m = 0, n = 1$ island, resonating at the reversal radius. Moreover, the ratio between the two perpendicular

transport terms at the edge, radial diffusion and toroidal convection, $D_r/v_\phi L_n$, is always in favor of the toroidal term, which is much larger than the radial one. This adds a new piece of information to the standard MARFE theory, which involves the ratio between parallel heat transport and perpendicular diffusion, $\kappa_\parallel/D_\perp$ [22].

The flow reversal, which takes place at $n/n_G \gtrsim 0.35$, is a precursor of the density limit, which in a strict sense is the impossibility of sustaining a discharge at $n \sim n_G$. The threshold for the precursor coincides with a change of regime in turbulent diffusion in the edge. In this sense, ORBIT shows that classical motion can explain the high-density behavior, while at low densities a turbulent transport is more likely to dominate the edge.

On the other hand, a sharp increase in $m = 0$ mode amplitude takes place at $n/n_G > 0.35$, associated with a modulation of the toroidal displacement $\delta_{m=0}$ which is the ultimate source of the $\boldsymbol{E}_r$ reversal. This suggests that the transition between the QSH and the MH states [6] plays a critical role, and is a strong precursor of the density limit phenomenology which takes place at $n \sim n_G$. The analysis of the edge topology in QSH shows an array of islands with the same periodicity of the dominant mode ($n = 7$), and X-points that act as electron pumps. The simulated ambipolar electric field in the edge is anyway always negative, with no flow reversal. The role of these X-points in QSH is matter of further study. The overall picture of the density limit in the RFP is therefore that a transition from a high-confinement to a low-confinement state takes place at $n/n_G \sim 0.35$, with associated toroidal inhomogeneity and unbalanced flows in the edge. This mechanism of modulation of $\boldsymbol{E}_r$ along the perpendicular angular direction could be of some relevance also for explaining the X-point MARFE in tokamaks: in tokamaks too the poloidal flow can give origin to convection terms $v_\theta L_n$ which can easily exceed radial diffusion.

From the experimental point of view, two types of experiments can be performed to ascertain the role of MHD: the first, to explore in more detail the known dependence of the $m = 0$ modes on the reversal parameter F and plasma current; the second, to perform ULq discharges at high density, where the $m = 0$ amplitude vanishes, by diagnosing in detail the possibility of exceeding the Greenwald density and paying a particular attention to the density profile. Wall conditioning with lithium is also a track which will be followed in the RFX-mod experimental campaign during year 2010.

References

[1] Greenwald M 2002 Density limits in toroidal plasmas *Plasma Phys. Control. Fusion* **44** R27–53
[2] Giannone L *et al* 2000 Physics of the density limit in the W7-AS stellarator *Plasma Phys. Control. Fusion* **42** 603–27

[3] Sonato P *et al* 2003 Machine modification for active MHD control in RFX *Fusion Eng. Des.* **66–68** 161–8

[4] Puiatti M E *et al* 2009 Helical equilibria and magnetic structures in the reversed field pinch and analogies to the tokamak and stellarator *Plasma Phys. Control. Fusion* **51** 124031

[5] Lorenzini R *et al* and RFX-mod team and collaborators 2009 Self-organized helical equilibria as a new paradigm for ohmically heated fusion plasmas *Nature Phys.* **5** 570–4

[6] Cappello S, Bonfiglio D, Escande D F, Guo S C, Alfier A and Lorenzini R 2008 The Reversed Field Pinch toward magnetic order: a genuine self-organization *2008 Varenna Conf. on Theory of Fusion Plasmas (Varenna Theory 2008) (Varenna, Italy, 25–29 August 2008), AIP Conf. Proc.* **1069** 27–39

[7] Lorenzini R, Terranova D, Alfier A, Innocente P, Martines E, Pasqualotto R and Zanca P 2008 Single-helical-axis states in reversed-field-pinch plasmas *Phys. Rev. Lett.* **101** 025005

[8] Valisa M, Frassinetti L, Paccagnella R, Puiatti M E, Sattin F, Scarin P, Spizzo G, Spolaore M, Vianello N and the RFX team 2006 Edge transport properties of RFX-mod approaching the Greenwald density limit *Proc. 21st IAEA Fusion Energy Conf. (Chengdu, China)* vol IAEA-CN-149 (Vienna: IAEA) pp EX/P3–17, available online at http://www-naweb.iaea.org/napc/physics/FEC/FEC2006/papers/ex_p3-17.pdf

[9] Puiatti M E *et al* 2009 High density physics in reversed field pinches: comparison with tokamaks and stellarators *Nucl. Fusion* **49** 045012

[10] Puiatti M E *et al* 2009 High density limit in reversed field pinches *Phys. Plasmas* **16** 012505

[11] Lipschultz B 1987 Review of MARFE phenomena in tokamaks *J. Nucl. Mater.* **145–147** 15–25

[12] Doyle E J (Chair Transport Physics) *et al*, ITPA Transport Physics Topical Group, ITPA Confinement Database, Modelling Topical Group, ITPA Pedestal and Edge Topical Group 2007 ITER Physics Basis, Chapter 2: Plasma confinement and transport *Nucl. Fusion* **47** S18–S127

[13] Wesson J A *et al* 1989 Disruptions in JET *Nucl. Fusion* **29** 641–66

[14] Schüller F C 1995 Disruptions in tokamaks *Plasma Phys. Control. Fusion* **37** A135

[15] Valisa M and the RFX team 2004 The Greenwald density limit in the Reverse Field Pinch *Proc. 20th IAEA Fusion Energy Conf. (Vilamoura, Portugal)* vol IAEA-CN-116 (Vienna: IAEA) pp EX/P4–13, available online at http://www-naweb.iaea.org/napc/physics/fec/fec2004/papers/ex_p4-13.pdf

[16] LaBombard B, Boivin R L, Greenwald M, Hughes J, Lipschultz B, Mossessian D, Pitcher C S, Terry J L and Zweben S J (Alcator Group) 2001 Particle transport in the scrape-off layer and its relationship to discharge density limit in Alcator C-mod *Phys. Plasmas* **8** 2107–17

[17] Miyazawa J *et al* and the LHD Experimental Group 2008 Density limit study focusing on the edge plasma parameters in LHD *Nucl. Fusion* **48** 015003

[18] de Vries P C, Rapp J, Schüller F C and Tokar' M G V 1998 Influence of recycling on the density limit in TEXTOR-94 *Phys. Rev. Lett.* **80** 3519–22

[19] Wyman M D *et al* 2008 High-beta, improved confinement reversed-field pinch plasmas at high density *Phys. Plasmas* **15** 010701

[20] Wyman M D *et al* 2009 Plasma behaviour at high β and high density in the Madison Symmetric Torus RFP *Nucl. Fusion* **49** 015003

[21] Rapp J *et al* 2001 Operational limits under different wall conditions on TEXTOR-94 *J. Nucl. Mater.* **290–293** 1148–54

[22] Tokar M Z, Rapp J, Reiser D, Samm U, Schüller F C, Sergienko G and de Vries P C 1999 Localized recycling as a trigger of MARFE *J. Nucl. Mater.* **266–269** 958–62

[23] Mazzitelli G *et al* 2007 Experiments on FTU with a liquid lithium limiter *Proc. of the 34th EPS Conf. on Plasma Physics (Warsaw, Poland, 2–6 July 2007)* vol 31F ed P Gasior and J Wołowski (Petit Lancy: European Physical Society) O-2.001, http://epsppd.epfl.ch/Warsaw/pdf/O2_001.pdf

[24] Apicella M L, Mazzitelli G, Pericoli Ridolfini V, Lazarev V, Alekseyev A, Vertkov A and Zagórski R 2007 First experiments with lithium limiter on FTU *J. Nucl. Mater.* **363–365** 1346–51

[25] White R B and Chance M S 1984 Hamiltonian guiding center drift orbit calculation for plasmas of arbitrary cross section *Phys. Fluids* **27** 2455–67

[26] Spizzo G, Cappello S, Cravotta A, Escande D F, Predebon I, Marrelli L, Martin P and White R B 2006 Transport barrier inside the reversal surface in the chaotic regime of the reversed-field pinch *Phys. Rev. Lett.* **96** 025001

[27] Marrelli L *et al* 2007 Magnetic self organization, MHD active control and confinement in RFX-mod *Plasma Phys. Control. Fusion* **49** B359–69

[28] Bartiromo R *et al* 2000 Analysis of the high density limits in the RFX high current regimes *Proc. of the 27th EPS Conf. on Plasma Physics (Budapest, Hungary, 12–16 June 2000)* vol 24B ed K Szegö *et al* (Petit Lancy: European Physical Society) pp 1380–3, http://epsppd.epfl.ch/Buda/pdf/p4_031.pdf

[29] Alfier A and Pasqualotto R 2007 New Thomson scattering diagnostic on RFX-mod *Rev. Sci. Instrum.* **78** 013505

[30] Alfier A, Fassina A, Auriemma F, Spizzo G and Pasqualotto R 2010 Electron pressure measurements in the outer region of rfx-mod with the upgraded edge thomson scattering diagnostic *Plasma Phys. Control. Fusion* **52** 035004

[31] Bonomo F, Alfier A, Gobbin M, Auriemma F, Franz P, Marrelli L, Pasqualotto R, Spizzo G and Terranova D 2009 2D characterization of core thermal topology changes in controlled RFX-mod QSH states *Nucl. Fusion* **49** 045011

[32] Kusano K, Tamano T and Sato T 1991 MHD simulations of the toroidal phase locking mechanism in a reversed field pinch plasma *Nucl. Fusion* **31** 1923–32

[33] Carraro L, Costa S, Puiatti M E, Sattin F, Scarin P and Valisa M 2000 Reconstruction of the radiation emitted by the intrinsic impurities in the RFX reversed field pinch *Plasma Phys. Control. Fusion* **42** 731–41

[34] Wesson J, Gowers C, Han W, Mast F, Nave F, Turner M and Watkins M 1985 Density limit disruptions in JET *12th EPS Conf. on Controlled Fusion and Plasma Physics (Budapest, Hungary, 2–6 September 1985)* vol 9F, ed L Pócs and A Montivai (Petit Lancy: European Physical Society) p 147

[35] Zanca P *et al* 2001 Analysis of phase locking of tearing modes in reversed field pinch plasmas *Phys. Plasmas* **8** 516–24

[36] Cappello S and Biskamp D 1996 Reconnection processes and scaling laws in reversed field pinch magnetohydrodynamics *Nucl. Fusion* **36** 571–81

[37] Cappello S and Biskamp D 1996 Nonlinear MHD sustainment dynamics of the reversed field pinch (RFP) configuration at different values of the pinch parameter *1996 Int. Conf. on Plasma Physics (ICPP 96 Nagoya) (Nagoya, Japan, 9–13 September 1996)* vol 1, ed P E Stott *et al* (Bristol: Institute of Physics Publishing) pp 854–7

[38] Zanca P and Martini S 2001 $m = 0$ perturbations of the magnetic surfaces in an RFP *Plasma Phys. Control. Fusion* **43** 121–35

[39] Rapp J, Fundamenski W, Ingesson L C, Jachmich S, Huber A, Matthews G F, Morgan P, Stamp M F and JET-EFDA Contributors 2008 Septum assessment of the JET gas box divertor *Plasma Phys. Control. Fusion* **50** 095015

[40] Cappello S and Escande D F 2000 Bifurcation in viscoresistive MHD: the Hartmann number and the reversed field pinch *Phys. Rev. Lett.* **85** 3838–41

[41] Bonfiglio D, Cappello S, Piovan R, Zanotto L and Zuin M 2008 3D nonlinear MHD simulations of ultra-low q plasmas *Nucl. Fusion* **48** 115010

[42] Antoni V, Buffa A, Giudicotti L, Martini S, Ortolani S, Puiatti M E and Scarin P 1983 Temperature measurement on reversed field pinch in the ETA BETA II experiment *Workshop on Mirror-based and Field-reversed Approaches to Magnetic Fusion (Varenna (Como), Italy, 7–17 September 1983)* ed R F Post *et al*, International School of Plasma Physics, Monotypia Franchi, Città di Castello (Perugia), Italy pp 135–59

[43] Agostini M, Cavazzana R, Scarin P and Serianni G 2006 Operation of the gas-puff imaging diagnostic in the RFX-mod device *Rev. Sci. Instrum.* **77** 10E513

[44] Serianni G, Baker W and Dal Bello S 2003 High-spatial resolution edge electrostatic probe system for RFX *Rev. Sci. Instrum.* **74** 1558–62

[45] Martin P *et al* 1997 Soft x-ray and bolometric tomography in RFX *Rev. Sci. Instrum.* **68** 1256–60

[46] Scarin P, Agostini M, Cavazzana R, Sattin F, Serianni G, Spolaore M and Vianello N 2009 Edge turbulence scaling in RFX-mod as measured using GPI diagnostic *J. Nucl. Mater.* **390–391** 444–7

[47] Terry P W 2000 Suppression of turbulence and transport by sheared flow *Rev. Mod. Phys.* **72** 109–65

[48] Zaniol B, Carraro L, Gazza E, Predebon I, Puiatti M E, Scarin P, Spizzo G and Valisa M 2007 Impurity flow studies in RFX-mod operation with reduced MHD mode activity *Proc. of the 34th EPS Conf. on Plasma Physics (Warsaw, Poland, 2–6 July 2007)* vol 31F, ed P Gasior and J Wołowski (Petit Lancy: European Physical Society) P-1.082, http://epsppd.epfl.ch/Warsaw/pdf/P1_082.pdf

[49] Carraro L, Puiatti M E, Sattin F, Scarin P, Spolaore M, Valisa M, Zaniol B and Zanca P 2003 Plasma–wall interactions and radial electric fields in the reversed field pinch RFX *J. Nucl. Mater.* **313–316** 976–9

[50] Marrelli L, Zanca P, Martin P, Martini S and Murari A 1999 Edge localised asymmetric radiative phenomena in RFX *J. Nucl. Mater.* **266–269** 877–83

[51] Spolaore M, Antoni V, Cavazzana R, Regnoli G, Serianni G, Spada E, Vianello N, Bergsåker H and Drake J R 2002 Effects of $E \times B$ velocity shear on electrostatic structures *Phys. Plasmas* **9** 4110–3

[52] Scarin P, Agostini M, Cavazzana R, Sattin F, Serianni G and Vianello N 2007 Edge turbulence in RFX-mod virtual-shell discharges *J. Nucl. Mater.* **363–365** 669–73

[53] Temple D, Meyer H, Scannell R and Conway N J 2009 The radial electric field of MAST *Proc. of the 36th EPS Conf. on Plasma Physics (Sofia, Bulgaria, June 19–July 3 2009)* vol 33E, ed M Mateev and E Benova (Petit Lancy: European Physical Society) P5.191, http://epsppd.epfl.ch/Sofia/pdf/P5_191.pdf

[54] Hess W R, DeMichelis C, Mattioli M, Clairet F, Druetta M, Grosman A, Guirlet R, Hutter T, Lasalle J and Monier-Garbet P 1995 Experimental study of ergodic edge plasmas with marfes in tore supra *Plasma Phys. Control. Fusion* **37** 951

[55] Xu Y *et al* 2006 Influence of the static dynamic ergodic divertor on edge turbulence properties in textor *Phys. Rev. Lett.* **97** 165003

[56] Xu Y *et al* and the TEXTOR Team 2007 Edge turbulence during the static dynamic ergodic divertor experiments in textor *Nucl. Fusion* **47** 1696

[57] Carraro L, Puiatti M E, Sattin F, Scarin P and Valisa M 1998 Toroidal and poloidal plasma rotation in the reversed field pinch RFX *Plasma Phys. Control. Fusion* **40** 1021–34

[58] White R B 2006 *The Theory of Toroidally Confined Plasmas* 2nd edn (London: Imperial College Press) p 15

[59] Lichtenberg A J and Lieberman M A 1992 *Regular and Chaotic Dynamics* 2nd edn (New York: Springer) p 305

[60] Golant V E, Žilinskij A P and Sacharov S E 1980 *Fundamentals of Plasma Physics* 1st edn (*Wiley Series in Plasma Physics*) (New York: Wiley) pp 217–9

[61] Gobbin M, Marrelli L and White R B 2009 Numerical studies of transport mechanisms in RFX-mod low magnetic chaos regimes *Plasma Phys. Control. Fusion* **51** 065010

[62] Antoni V, Desideri D, Martines E, Serianni G and Tramontin L 1997 Plasma potential well and velocity shear layer at the edge of reversed field pinch plasmas *Phys. Rev. Lett.* **79** 4814–7

[63] Predebon I, Marrelli L, White R B and Martin P 2004 Particle-transport analysis in reversed field pinch helical states *Phys. Rev. Lett.* **93** 145001

[64] Vianello N *et al* and the RFX-mod Team 2009 Transport mechanisms in the outer region of RFX-mod *Nucl. Fusion* **49** 045008

[65] Liang Y *et al* 2005 Influence of the dynamic ergodic divertor on the density limit in textor *Phys. Rev. Lett.* **94** 105003

[66] Agostini M, Scarin P, Cavazzana R, Sattin F, Serianni G, Spolaore M and Vianello N 2009 Edge turbulence characterization in RFX-mod with optical diagnostics *Plasma Phys. Control. Fusion* **51** 105003

[67] Martines E, Lorenzini R, Momo B, Munaretto S, Innocente P and Spolaore M 2010 The plasma boundary in single helical axis RFP plasmas *Nucl. Fusion* **50** 035014

[68] Puiatti M E *et al* 2001 Plasma rotation and structure of the radial electric field in RFX *J. Nucl. Mater.* **290–293** 696–700

[69] Bartiromo R 1998 Plasma rotation and finite larmor radius losses in a reversed field pinch *Phys. Plasmas* **5** 3342–9

[70] Agostini M *et al* 2009 Plasma edge properties in different magnetic topologies in the RFX-mod device *Proc. of the 36th EPS Conf. on Plasma Physics (Sofia, Bulgaria, June 19–July 3 2009)* vol 33E, ed M Mateev and E Benova (Petit Lancy: European Physical Society) P-2.179, http://epsppd.epfl.ch/Sofia/pdf/P2_179.pdf

[71] Vlad M, Spineanu F, Misguich J H and Balescu R 2000 Collisional effects on diffusion scaling laws in electrostatic turbulence *Phys. Rev. E* **61** 3023–32